



Nanoscale

ARTICLE

Turning Antiferromagnetic $\text{Sm}_{0.34}\text{Sr}_{0.66}\text{MnO}_3$ into a 140 K Ferromagnet Using a Nanocomposite Strain Tuning Approach

Ady Suwardi,^a Bhagwati Prasad,^a Shin Buhm Lee,^a Eun-Mi Choi,^a Ping Lu,^b Wenrui Zhang,^c Leigang Li,^c Mark Blamire,^a Quanxi Jia,^d Haiyan Wang,^c Kui Yao^e and Judith L. MacManus-Driscoll^{*a}

Received 00th January 20xx,
Accepted 00th January 20xx

DOI: 10.1039/x0xx00000x

www.rsc.org/

Ferromagnetic insulating thin films of $\text{Sm}_{0.34}\text{Sr}_{0.66}\text{MnO}_3$ (SSMO) on (001) SrTiO_3 substrates with T_C of 140 K were formed in self-assembled epitaxial nanocomposite thin films. The high T_C ferromagnetism was enabled through vertical epitaxy of the SSMO matrix with embedded, stiff, ~ 40 nm Sm_2O_3 nanopillars giving a c/a ratio close to 1 in the SSMO. In contrast, bulk and single phase SSMO films of the same composition have much stronger tetragonal distortion, the bulk having $c/a > 1$ and the films having $c/a < 1$, both of which give rise to antiferromagnetic coupling. The work demonstrates a unique and simple route to creating ferromagnetic insulators for spintronics applications where currently available ferromagnetic insulators are either hard to grow and/or have very low T_C .

Introduction

Ferromagnetic insulators (FMIs) are of great research interest due to the rare combination of ferromagnetism and insulating characteristics which are needed for oxide spintronics and multiferroics.¹⁻³ FMIs can be used in spin-filter barriers in magnetic tunnel junctions (MTJs). They are also an important parent compounds for creating multiferroics, in which the coexistence of ferromagnetism and ferroelectricity leads to magneto-dielectric coupling.⁴⁻⁷

There are few spin-filter materials with very high efficiency. EuS and EuSe are rare examples, but the low T_C s (16.6 K for EuS and 4.6 K for EuSe) of these materials limits their application to liquid helium temperatures.^{5, 8} In order to realize higher temperature applications, EuO has been investigated (T_C of 69 K). Nevertheless, the challenging growth conditions hinder its use.⁹ Other promising candidates with high T_C including ferrites, but these are not without their own problems. For instance, rare-earth nitrides suffer stability problems due to rapid oxidation in air¹⁰ while ferrites, although having above room temperature T_C ¹¹, have complex spinel structures, making it difficult for integration into tunnel hetero-structures made of half-metallic ferromagnetic perovskites such as $\text{La}_{0.67}\text{Sr}_{0.33}\text{MnO}_3$

(LSMO).¹² Consequently, new practical FMIs are strongly needed. Perovskites are excellent candidates as they are chemically and structurally compatible with numerous oxide electrodes.¹³

Transition metal oxide perovskites are interesting because of their wide variety of structural, magnetic and transport properties.^{14, 15} For example, the $\text{RE}_{1-x}\text{AE}_x\text{MnO}_3$ (RE and AE represent a trivalent rare earth and a divalent alkaline earth elements, respectively) systems exhibit a very rich electronic and magnetic phase diagram due to strong coupling between the charge, orbital and spin degrees of freedom.^{16, 17} However, only very few insulating perovskite manganites are ferromagnetic. Notable exceptions are BiMnO_3 and $\text{La}_{0.1}\text{Bi}_{0.9}\text{MnO}_3$ with T_C s of around 100 K. However, the growth of these materials is non-trivial.^{18, 19} $\text{Sm}_{1-x}\text{Sr}_x\text{MnO}_3$ (SSMO), with $x = 0.1$ to $x = 0.3$, is another potential perovskite FMI with a maximum T_C also of ~ 100 K in bulk.²⁰ Recently, spin filter tunnel junctions based on SSMO were fabricated into devices,²¹ giving 75% spin polarization. However, the junctions operated mainly at a low temperature of 5 K.²² Thus despite promising bulk properties, in strained films wide deviations in the ferromagnetic properties result.²³⁻²⁸ Indeed, SSMO, of low band width, has great sensitivity of its physical properties to both strain and composition.²⁹ Even with minimization of substrate-induced strain using buffer layers and highly lattice matching substrates^{23, 26, 27}, properties are still very different to bulk values because of incomplete strain relaxation and also possibly because of oxygen vacancy strain-accommodating defects.³⁰ More recently, studies have focused on several perovskite systems where strain *enhances* T_C .³¹⁻³⁴ However, again strain relaxation with film thickness leads to non-uniform properties through the film.³⁵

The objective of this work is to use a nanocomposite thin film approach to create a stable ferromagnetic insulating phase

^a Department of Materials Science and Metallurgy, University of Cambridge, 27 Charles Babbage Road, Cambridge, CB3 0FS, UK

^b Sandia National Laboratories, Albuquerque, New Mexico 87185, USA

^c Department of Electrical and Computer Engineering, Texas A&M University, College Station, TX 77843, USA

^d Center for Integrated Nanotechnologies (CINT), Los Alamos National Laboratory, Los Alamos, New Mexico 87545, USA

^e Institute of Materials Research and Engineering, A*STAR (Agency for Science, Technology and Research), 2 Fusionopolis Way, Innovis, #08-03 Singapore 138634

* Corresponding author email : jlid35@cam.ac.uk

| Properties | Sm _{0.34} Sr _{0.66} MnO ₃ in nanocomposite film | Single phase Sm _{0.34} Sr _{0.66} MnO ₃ film | Bulk Sm _{0.37} Sr _{0.63} MnO ₃ ³⁶ (pseudo-cubic) |
|------------------------------------|--|--|--|
| Thickness | 120 nm | 100 nm | N.A. |
| a (Å) | 3.846 ± 0.016 | 3.876 ± 0.009 | 3.785 |
| c (Å) | 3.819 ± 0.008 | 3.756 ± 0.005 | 3.899 |
| In-plane strain (%) | 1.61 ± 0.42 ^a | 2.40 ± 0.24 ^a | N.A. |
| Out-of-plane strain (%) | -2.05 ± 0.21 ^a | -3.67 ± 0.13 ^a | N.A. |
| Tetragonality (c/a) | 0.993 ± 0.024 | 0.969 ± 0.014 | 1.030 |
| Magnetic properties | Ferromagnetic | Antiferromagnetic | Antiferromagnetic |
| T _C /T _N (K) | T _C = 140 | T _N = 100 | T _N = 250 |
| Electrical properties | Insulating | Insulating | Insulating |

Table 1. Properties of nanocomposite films compared to single phase films and bulk.
^aStrain calculated relative to bulk Sm_{0.37}Sr_{0.63}MnO₃

which is not susceptible to substrate strain, which can be formed easily and which has uniform properties through thickness. In nanocomposite films, strain is controlled in a matrix by using a stiff strain-controlling second phase pillar in the film which controls the *out-of-plane* strain.³⁷ In this case, the strain controlling pillars are Sm₂O₃ (E_{SmO} = 240 GPa³⁸ vs E_{SSMO} = 130-160 GPa³⁹, where E is the average elastic modulus) and the matrix is SSMO.

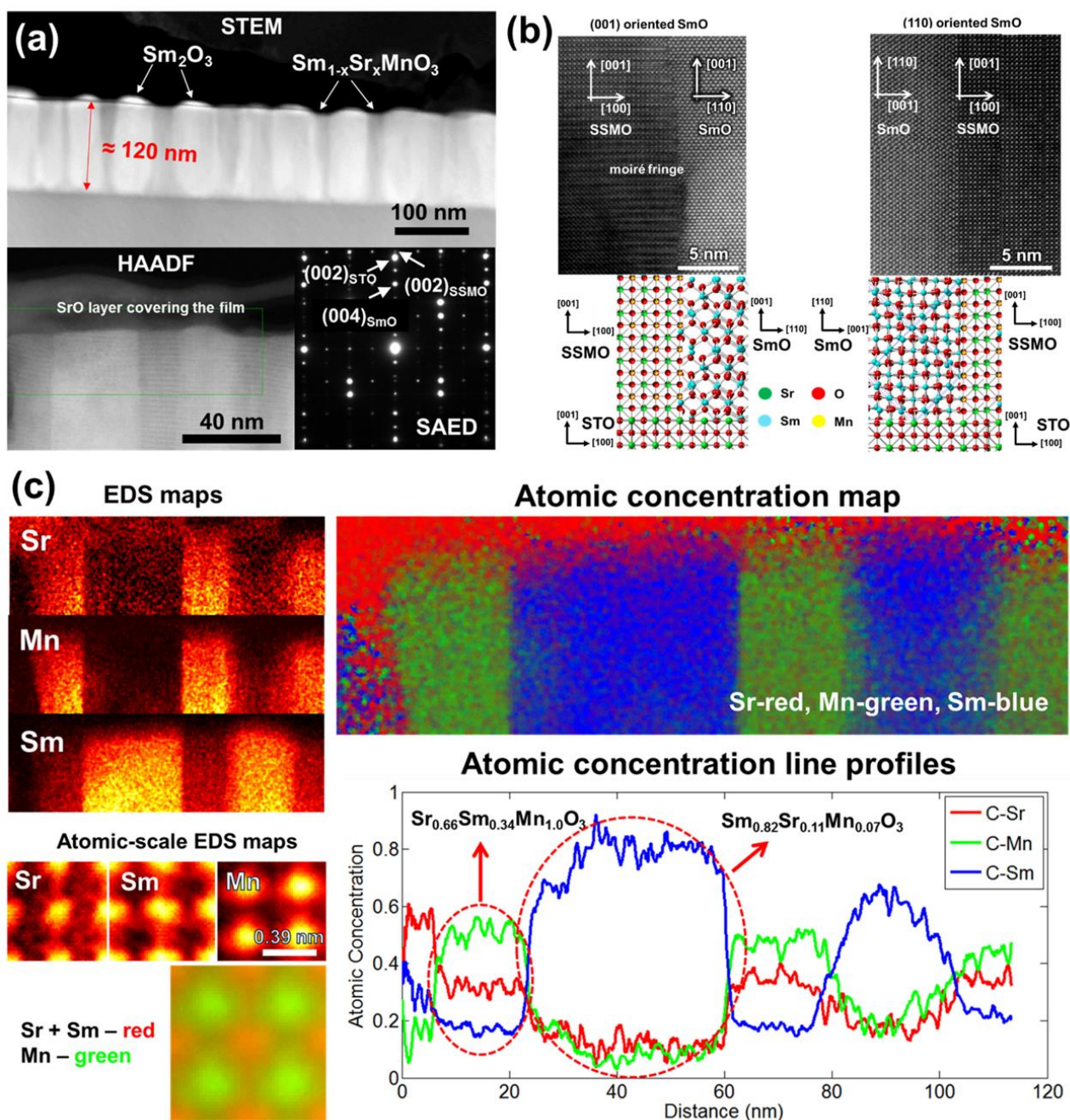


Figure 1. (a) High resolution cross sectional TEM image of the nanocomposite film (top). High-angle annular dark field (HAADF) image (bottom left) as well as selected area electron diffraction (SAED) (bottom right). (b) High resolution TEM image showing the interface between nanopyllar and matrix (top). Crystal orientation representation of nanopyllar and matrix as well as substrate (bottom). (c) EDS map showing the compositions of nanopyllars and matrix (top left and top right). Atomic-scale EDS maps (bottom left) showing Sr and Sm occupy of the same sites in the perovskite lattice and atomic concentration line profile (bottom right) showing the lateral compositions of nanopyllars and matrix.

In such nanocomposite films, in the less-stiff matrix, the *out-of-plane* strain is controlled by vertical epitaxy, while the *in-plane* strain is determined by a combination of heteroepitaxy with the substrate as well by elastic interactions with the stiff nanopyllars. Hence the relative mechanical properties (e.g. elastic moduli and thermal expansion coefficients) of the two materials in the composite film are important for controlling the *in-plane* strain.⁴⁰ Overall, a uniform and unconventional strain

state can be induced in the matrix phase in *thick* ($\sim\mu\text{m}$) nanocomposite films, something that is not possible in conventional thin films whose lattice parameters are dependent on planar epitaxy, with strain beginning to relax above just a few nm. In addition, for conventional films there is the problem of limited availability and high cost of single crystal substrates for precisely tuning lattice parameters in the films.

Results and Discussion

Since Sm readily substitutes into SrMnO_3 , it was expected that Sm would displace Sr in the SrMnO_3 matrix, leading to Sr expulsion from the film. Fig 1(a) (top panel) shows scanning transmission electron microscopy (STEM) image of a 120 nm thick nanocomposite showing the SmO nano-pillars embedded in the SSMO matrix. The bottom left panel of Fig 1(a) shows a high angle annular dark field (HAADF) image. This image reveals a darker SrO phase on the surface of the nanocomposite film. The presence of the surface SrO in our films is consistent with previous studies showing Sr migration to film surfaces to give poorly crystalline precipitates⁴¹. The selected area electron diffraction (SAED) pattern in the bottom right panel of Fig. 1(a) shows the high quality crystallinity of the STO substrate as well as the SmO and SSMO phases in the film.

A high resolution cross-sectional TEM image of a nanocomposite film shows a clean and sharp interface between the SmO nano-pillars and the SSMO matrix (see Fig 1(b)). Two different orientations of the SmO nano-pillars were observed, (110) and (001) while only one orientation of SSMO was

observed, (001). As shown in the schematic crystal in the lower part of Fig. 1(b), the (110) SmO phase was oriented with the STO substrate *in-plane* with $[110] \text{ SmO} \parallel [100] \text{ STO}$. On the other hand, the (001) SmO was oriented *in-plane* with $[100] \text{ SmO} \parallel [100] \text{ STO}$. The SSMO phase was oriented *in-plane* with $[100] \text{ SSMO} \parallel [100] \text{ STO}$.

The occurrence of the (110) orientation of SmO in the nanocomposite film is different to the case of single phase SmO films grown on (001) STO which are typically (001) oriented.⁴² The reason for this difference is that *vertical* epitaxial lattice matching between $[110] \text{ SmO}$ and $[001] \text{ SSMO}$ (0.9% misfit) in the (110) SmO films is much lower than the misfit between $[001] \text{ SmO}$ and $[001] \text{ SSMO}$ (6.6% misfit) in the (001) SmO films. Fig. 1(c) shows compositional characterization of the nanocomposite films by EDS, by atomic-scale EDS, by using atomic concentration maps, as by using atomic concentration line profiles. In the EDS maps, very sharp and clean interfaces can be observed from the bright regions for both Sr and Mn in the same area, with the bright region for Sm being in the adjacent area. The atomic-scale EDS maps shows direct

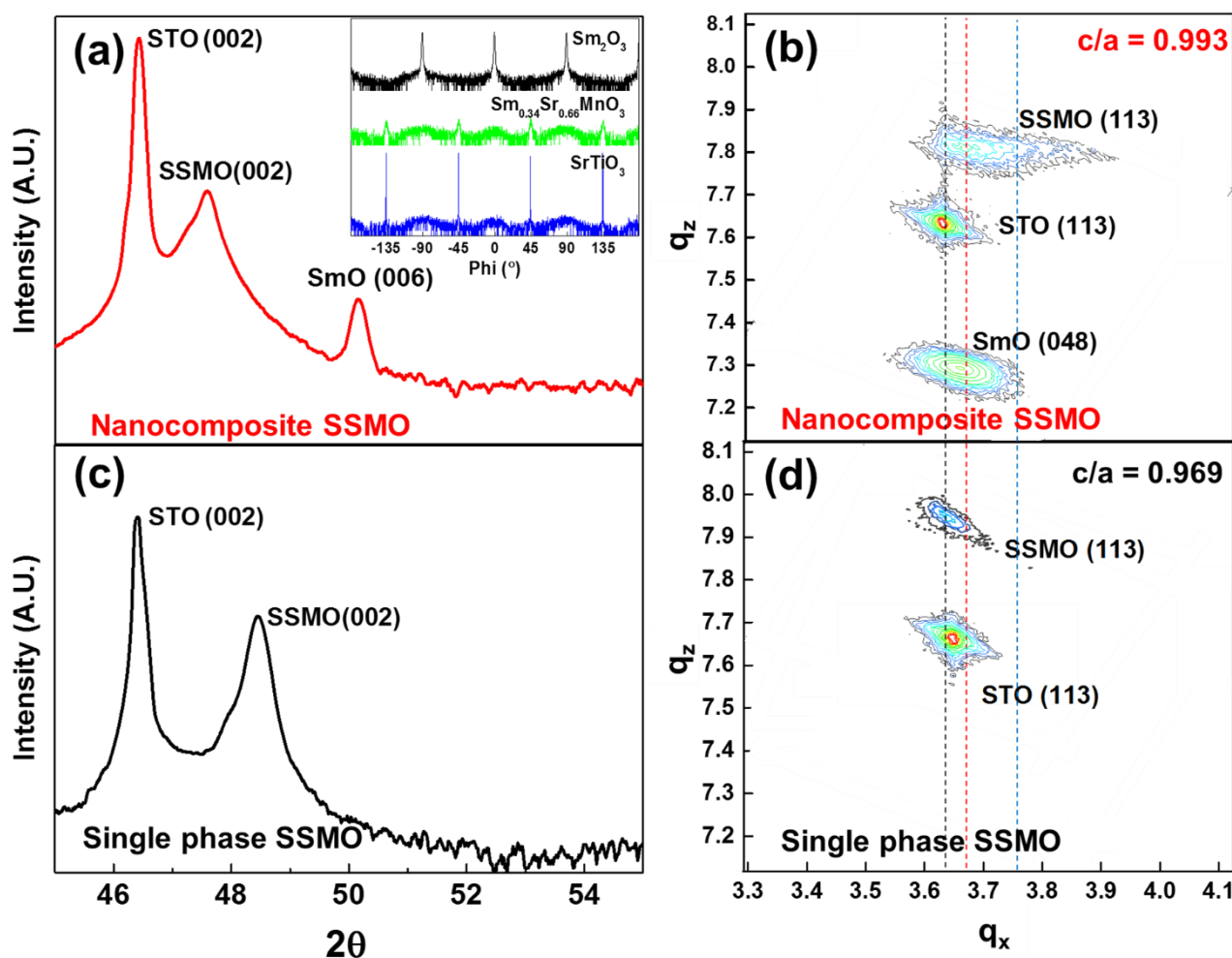


Figure 2. (a) 2θ - ω XRD scan of nanocomposite film showing the presence of SmO and SSMO phases and STO substrate, all with (001) orientation. Inset shows a phi-scan, revealing the different *in-plane* orientations of SmO and SSMO with respect to the STO substrate. (b) RSM of the nanocomposite film with vertical dashed lines indicating the centers of the peaks along q_x . (c) 2θ - ω XRD scan of a single phase SSMO film showing the presence of the SSMO film and the STO substrate, both with (001) orientation. (d) RSM of single phase SSMO film showing close alignment along q_x of the SSMO (113) peak with the STO (113) peak as a result of epitaxial growth which causes the SSMO *in-plane* lattice parameter to be equivalent to the STO *in-plane* lattice parameter.

evidence of Sm substitution onto the Sr site. The atomic concentration maps and line profiles shows the distinct nanopillars of composition $\text{Sm}_{0.82}\text{Sr}_{0.11}\text{Mn}_{0.07}\text{O}_3$ and the matrix of composition $\text{Sm}_{0.34}\text{Sr}_{0.66}\text{MnO}_3$. Hence, there is a $\sim 11\%$ substitution of Sr onto Sm_2O_3 and $\sim 34\%$ of Sm onto the Sr site in SrMnO_3 .

2θ - ω XRD scans of the nanocomposite films are shown in Fig. 2. Sharp peaks of SSMO (002) and SmO (006) are observed in the Bragg-Brentano scan in Fig. 2(a) with some overlapping of the

crystallinity of the SrO phase on top of the nanocomposite film, even though it was observed in the high angle annular dark field (HAADF) image of Fig. 1(a), it was not observable by XRD in Fig. 2.

X-ray phi-scans of the STO substrate and the SSMO and SmO peaks in the nanocomposite (inset of Fig. 2 (a)) show a cube-on-cube orientation of the SSMO on STO while the SmO shows a 45° *in-plane* rotation with respect to the STO substrate, consistent with the high resolution TEM images. Fig. 2(b) shows

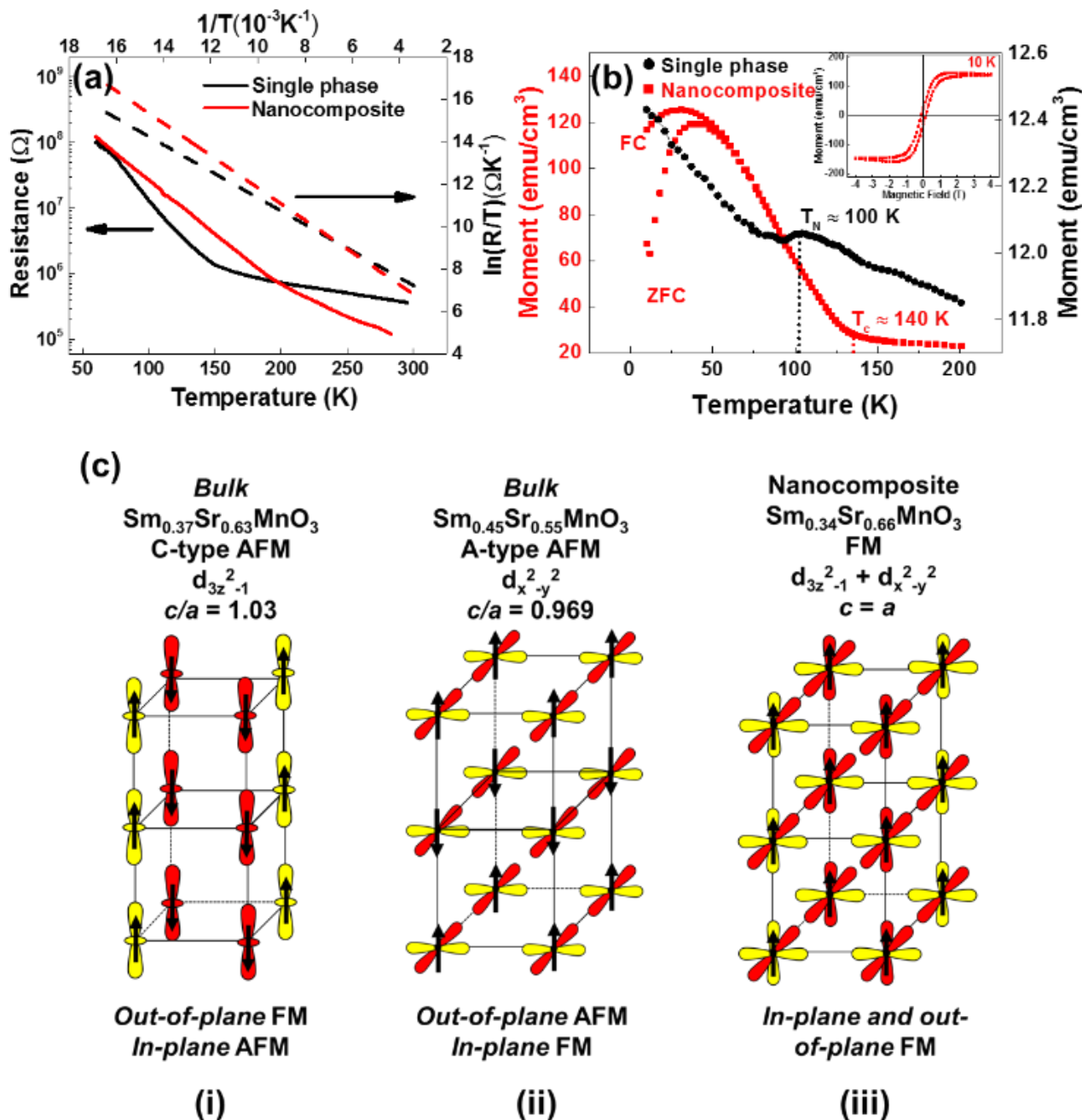


Figure 3. (a) Resistance vs temperature plot comparing nanocomposite to single phase film. The dotted lines in the plot shows linear fitting of $1/T$ vs $\ln(R/T)$. (b) Magnetization vs temperature plot comparing nanocomposite to single phase film. Inset shows magnetic hysteresis loop of the nanocomposite film. (c) Schematic diagram showing C-type and A-type AFM orbitals as well as FM orbitals with DE denoting double exchange coupling and SE denotes super-exchange coupling.

SSMO (002) and STO (001) peaks. No peaks associated with (110) SmO were observed due to the overlapping of SmO (440) with the STO (002) substrate peak. Owing to the poor

a reciprocal space map (RSM) of the nanocomposite film revealing the strain states of the phases in the nanocomposite film. As shown by the vertical dashed lined, q_x of the SSMO (113)

peak is shifted to the left compared to bulk SSMO, indicating a higher *a*-axis in the nanocomposite film compared to bulk. For comparison, Fig. 2(c) shows a 2θ - ω scan for a single phase SSMO film of the same thickness (~ 100 nm). In the 2θ - ω scan the (002) SSMO peak is at a higher 2θ value of 48.4° compared to 47.6° for the nanocomposite, indicating that the nanocomposite film has a higher *c* parameter than the single phase film. Fig. 2(d) shows a reciprocal space map (RSM) of the single phase film. The SSMO (113) peak along q_x is displaced further from the bulk SSMO position and hence the *a*-axis is larger than the one in the nanocomposite film. The different strain states obtained in the nanocomposite and single phase SSMO films are analyzed and discussed below.

The *in-plane* lattice parameters of the $\text{Sm}_{0.34}\text{Sr}_{0.66}\text{MnO}_3$ phase in both the nanocomposite film and single phase SSMO films were estimated by first determining the *out-of-plane* parameter from the 2θ - ω scans, and then by using this value to extract the *in-plane* lattice parameter obtained from the RSM (113) peak. As shown in Table 1, the *in-plane* and *out-of-plane* lattice parameters in the nanocomposite film are 3.846 ± 0.016 Å and 3.819 ± 0.008 Å, respectively. These values are $1.61 \pm 0.42\%$ in tension *in-plane* and $-2.05 \pm 0.21\%$ in compression *out-of-plane* relative to bulk $\text{Sm}_{0.37}\text{Sr}_{0.63}\text{MnO}_3$, giving *c/a* of 0.993 ± 0.024 . In contrast, the *in-plane* and *out-of-plane* lattice parameters for the single phase SSMO film are 3.876 ± 0.009 Å and 3.756 ± 0.005 Å, respectively. These values are $2.40 \pm 0.24\%$ in tension *in-plane* and $-3.67 \pm 0.13\%$ in compression *out-of-plane* relative to bulk $\text{Sm}_{0.37}\text{Sr}_{0.63}\text{MnO}_3$, giving *c/a* of 0.969 ± 0.014 . The higher level of strain and overall low *c/a* in the single phase film arises because of the *in-plane* epitaxial straining from the STO substrate ($a = 3.905$ Å). The partial relaxation of the *in-plane* lattice parameter to 3.876 Å is expected owing to the relatively thick film. The *out-of-plane* compression arises through elastic strain to conserve the cell volume.

On the other hand, in the nanocomposite film the *out-of-plane* compression arises from vertical epitaxy with the stiff Sm_2O_3 nano-pillars. Here, for the (001) Sm_2O_3 orientation 3 unit cells of SSMO match with 1 unit cell of SmO (3×3.819 Å || 1×10.93 Å), and for the (110) SmO orientation, 4 unit cells of SSMO match with 1 unit cell of SmO (4×3.819 Å || $1 \times 10.93 \times \sqrt{2}$ Å). The *in-plane* tension arises because upon cooling the film from the growth temperature, the stiff Sm_2O_3 pillars with lower coefficient of thermal expansion cause the vertically epitaxially coupled $\text{Sm}_{0.34}\text{Sr}_{0.66}\text{MnO}_3$ to expand.⁴⁰ The tension is less in the composite film compared to the single phase SSMO films because of the different mechanism of the strain control.

Resistance vs. temperature plots comparing a nanocomposite film to a single phase SSMO film are shown in Fig. 3(a). An insulating profile was observed throughout the measurement temperature range. Below 50 K, the resistance of both films is beyond the measurement limit. The electrical conduction mechanism at high temperature follows the small polaron hopping (SPH) model.^{43, 44} The resistance as a function of temperature is given by $R(T) = A \cdot T \exp(E_A/k_B T)$, where E_A is the activation energy for conduction, T is the temperature and A is a constant. The activation energy E_A , is determined by using

linear fitting of the $\ln(R/T)$ vs $1/T$ (dotted line of Fig. 3(a)), giving 94 meV for the nanocomposite film and 84 meV for the single phase SSMO film. Both of these values are higher than the bulk SSMO value of 45–46 meV.⁴⁵ This is consistent with reduction of the electrical conduction because of strain in the films (and in the nanocomposite case, defects along the vertical interfaces between the two phases).

The comparative magnetic properties of the nanocomposite and single phase SSMO films are shown in Fig. 3(b). M vs T plots show ferromagnetism with a T_C of 140 K for the nanocomposite film. We note that in the literature the highest T_C value in the ferromagnetic insulating (FMI) Sr-doped SmMnO_3 system is 100 K²² which is for the optimally doped (25% Sr doped) composition, and so the T_C of the SSMO phase formed in our nanocomposite films is 40K higher than for any FMI Sr-doped SmMnO_3 phase. In addition, the T_C of our nanocomposite films is 10 K higher than for the ferromagnetic metal (FMM), Sr-doped SmMnO_3 (48% Sr).⁴⁶

A cluster-glass like behaviour with a strong bifurcation between the field-cooled (FC) and zero field-cooled (ZFC) at 50 K was observed and the proposed origin of this is discussed later.⁴⁷ The inset of Fig. 3(b) shows the magnetic hysteresis loop of M vs H at 10 K for the nanocomposite film. After subtracting the paramagnetic background from the substrate and Sm_2O_3 , a clear ferromagnetic hysteresis loop is obtained. The coercivity (H_C) and saturation magnetic moment (M_S) are 100 Oe and 146 emu/cm^3 ($1.93 \mu_B/\text{Mn}$), respectively. This is comparable to the optimum 25% Sr doped SmMnO_3 phase, mentioned above.²²

For the single phase SSMO films, AFM behavior was observed with a T_N of 100 K (Fig. 3(b)).²⁰ This is comparable to bulk $\text{Sm}_{0.34}\text{Sr}_{0.66}\text{MnO}_3$ which shows C-type antiferromagnet behaviour, although the T_N is higher for the bulk at ~ 220 K, consistent with the very different levels of tetragonal distortion (*c/a* = 0.969 for the single phase films, vs. 1.030 for the bulk, as shown in Table 1

). We now turn to the understanding of the magnetic properties for the plain versus nanocomposite films of this study. In doped manganites, magnetic interactions between the Mn atoms are determined by competitions between FM double exchange interactions and AFM super-exchange.⁴⁸ The origin of the magnetic properties in the nanocomposite films can be understood by first realising that the level of structural distortion strongly influences these interactions. With Jahn-Teller effects at play, small distortions of MnO_6 can stabilize either one of the e_g orbitals, $3z^2-r^2$ or x^2-y^2 . For *c/a* > 1 (*c/a* < 1), the MnO_6 octahedra are tensed (compressed) and consequently the $3z^2-r^2$ (x^2-y^2) orbitals are energetically favoured over the x^2-y^2 ($3z^2-r^2$) orbitals.

Hence, for *c/a* > 1 the $3z^2-r^2$ orbitals have a higher occupancy. This results in 1-D FM double exchange interactions along the *out-of-plane* direction. The 1-D FM columns are AFM owing to super-exchange coupling. This results in C-type AFM structure (as shown in Fig. 3(c)i). This is the case for bulk $\text{Sm}_{0.37}\text{Sr}_{0.63}\text{MnO}_3$, *c/a* = 1.03 (Table 1).

For *c/a* < 1, the x^2-y^2 orbitals have a higher occupancy. This leads to strong double exchange coupling in the MnO_2 planes

which strengthens the ferromagnetic ordering *in-plane*. At the same time, super-exchange coupling stabilizes the antiferromagnetic ordering in the *out-of-plane* direction. This results in an A-type AFM as shown in Fig. 3(c ii). This is the case for the single phase $\text{Sm}_{0.37}\text{Sr}_{0.63}\text{MnO}_3$ films, $c/a = 0.969$ (Table 1).

In our $\text{Sm}_{0.34}\text{Sr}_{0.66}\text{MnO}_3$ nanocomposite films, $c/a = 0.993 \pm 0.024$ (Table 1). Hence, the tetragonal distortion is reversed compared to the bulk value. Because c is close to a there is more or less equal occupation of the x^2-y^2 and $3z^2-r^2$ orbitals which produces double exchange interactions in both the *in-plane* and *out-of-plane* directions, thus leading to ferromagnetic ordering in 3-dimensions (as shown in Fig 3(c iii)).⁴⁸

As well as the extent of tetragonal distortion in the films, we should also consider the actual Mn-O-Mn bond lengths. This is because AFM super-exchange interactions depend on Mn-O distances more strongly than the FM double exchange interactions do. Hence, longer Mn-O bond lengths make the AFM super-exchange coupling weaker, whereas they influence the FM double exchange much less.⁴⁹ Hence, in our films FM double exchange dominates over AFM super-exchange, leading to the observed FM behavior. Overall, however, the AFM interactions in the film compete with the FM interactions. This competition explains the cluster glass-like behaviour in the M vs T plot below 50 K in Fig. 3(b).

On a final note, the creation of high T_c ferromagnetism in our nanocomposite films are achieved via strain coupling between two phases. The work parallels artificial super-lattice (SL) studies where magnetic phases are coupled to other phases in a parallel configuration. In the SL studies, strong enhancements of T_c have been found when the *in-plane* strain is controlled by lateral coupling of phases. A T_c of 650 K (increased by nearly 300K compared to bulk and plain films) has been observed for LSMO-BTO (with *in-plane* straining of the LSMO by 1%).⁵⁰ A key difference between the SL films and the nanocomposite films is that the nanocomposite films self-assemble rather than being made by a complex layering process.

In summary, in nanocomposite $\text{Sm}_{0.34}\text{Sr}_{0.66}\text{MnO}_3$ (SSMO) films using self-assembled vertical, strain controlling SmO nanopillars embedded in the SSMO matrix, a low c/a ratio is induced in the SSMO. Essentially, using nanocomposite films has enabled us to create a ferromagnetic insulator in a relatively thick film out of an otherwise antiferromagnetic insulator. The strain states (in both magnitude and uniformity) induced using the nanocomposite approach cannot be realised in single phase films and hence a new dimension for property control is realized by using these structures.

Experimental

Nanocomposite films of $\text{Sm}_{0.34}\text{Sr}_{0.66}\text{MnO}_3 - \text{Sm}_2\text{O}_3$ were grown on (001) SrTiO_3 substrates using pulsed laser deposition (PLD). The starting target materials for PLD were prepared using stoichiometric mixture of $\text{Sm}_2\text{O}_3 + \text{SrCO}_3 + \text{MnO}_2$ powders by solid state sintering at 1100°C for 6 hours. A Lambda Physik KrF excimer laser ($\lambda = 248$ nm) was used for target ablation. The laser energy density was set at 1 J/cm² with a target-to-

substrate distance of 4.5 cm and 1 Hz pulse repetition rate. The vertical nanocomposite films was grown at 750°C and 20 Pa oxygen pressure, followed by a short post deposition annealing at the same temperature for 30 minutes at 100 mbar oxygen atmosphere. The resulting thickness of the film is 120 nm.

A Panalytical high resolution X-ray diffractometer (with Cu K α radiation, a 2-bounce hybrid monochromator and 0.5 mm slit beam tunnel) was used to determine the phase and crystalline quality of the deposited films. Cross-sectional images of the film were taken with high resolution transmission electron microscopy (HRTEM). Platinum contacts were deposited by standard magnetron DC sputtering to serve as the top contact for electrical measurement. Magnetic properties were characterized using superconducting quantum interference device (SQUID).

Conclusions

Nanocomposite films containing $\text{Sm}_{0.34}\text{Sr}_{0.66}\text{MnO}_3$ were grown on SrTiO_3 (001) with 120 nm thickness. Stiff Sm_2O_3 nanopillars formed in the matrix of $\text{Sm}_{0.34}\text{Sr}_{0.66}\text{MnO}_3$, gave a unique strain state of lower *in-plane* tensile and *out-of-plane* compression than can otherwise be realized in single phase films. This leads to lower c/a value compared to both single phase films and to bulk. This c/a reduction leads to 140 K ferromagnetism and insulating behaviour. This work demonstrates a novel strain approach for tuning of magnetic properties in thin films.

Acknowledgements

This work was supported by the European Research Council (ERC) (Advanced Investigator grant ERC-2009-AdG-247276-NOVOX). A. Suwardi would also like to acknowledge the Agency for Science, Technology and Research (A*STAR) Singapore for funding his graduate studies. M. E. Vickers is thanked for her help with the X-ray characterization work and A. Sangle for helping with the initial experimental works.

Notes and references

- 1 W. Prellier, M. Singh and P. Murugavel, *Journal of Physics: Condensed Matter*, 2005, **17**, R803.
- 2 W. Eerenstein, N. Mathur and J. F. Scott, *nature*, 2006, **442**, 759-765.
- 3 R. Ramesh and N. A. Spaldin, *Nature materials*, 2007, **6**, 21-29.
- 4 J. Moodera, X. Hao, G. Gibson and R. Meservey, *Physical review letters*, 1988, **61**, 637.
- 5 P. LeClair, J. Ha, H. Swagten, J. Kohlhepp, C. Van de Vin and W. De Jonge, *Applied physics letters*, 2002, **80**, 625-627.
- 6 N. S. Rogado, J. Li, A. W. Sleight and M. A. Subramanian, *Advanced Materials*, 2005, **17**, 2225-2227.
- 7 M. Singh, K. Truong and P. Fournier, *Applied Physics Letters*, 2007, **91**, 2504.

- 8 J. S. Moodera, J. Nowak and R. J. van de Veerdonk, *Physical Review Letters*, 1998, **80**, 2941.
- 9 T. S. Santos and J. S. Moodera, *Physical Review B*, 2004, **69**, 241203.
- 10 F. Natali, B. J. Ruck, N. O. Plank, H. J. Trodahl, S. Granville, C. Meyer and W. R. Lambrecht, *Progress in Materials Science*, 2013, **58**, 1316-1360.
- 11 U. Lüders, M. Bibes, K. Bouzehouane, E. Jacquet, J.-P. Contour, S. Fusil, J.-F. Bobo, J. Fontcuberta, A. Barthélémy and A. Fert, *Applied physics letters*, 2006, **88**, 2505.
- 12 M. Bowen, M. Bibes, A. Barthélémy, J.-P. Contour, A. Anane, Y. Lemaitre and A. Fert, *Applied Physics Letters*, 2003, **82**, 233-235.
- 13 A. Haghiri-Gosnet and J. Renard, *Journal of Physics D: Applied Physics*, 2003, **36**, R127.
- 14 M. Bibes, J. E. Villegas and A. Barthelemy, *Advances in Physics*, 2011, **60**, 5-84.
- 15 H. Hwang, Y. Iwasa, M. Kawasaki, B. Keimer, N. Nagaosa and Y. Tokura, *Nature materials*, 2012, **11**, 103-113.
- 16 E. Dagotto, T. Hotta and A. Moreo, *Physics reports*, 2001, **344**, 1-153.
- 17 Y. Tokura and N. Nagaosa, *science*, 2000, **288**, 462-468.
- 18 M. Gajek, M. Bibes, A. Barthélémy, K. Bouzehouane, S. Fusil, M. Varela, J. Fontcuberta and A. Fert, *Physical Review B*, 2005, **72**, 020406.
- 19 M. Gajek, M. Bibes, S. Fusil, K. Bouzehouane, J. Fontcuberta, A. Barthelemy and A. Fert, *Nature materials*, 2007, **6**, 296-302.
- 20 A. Kurbakov, A. Lazuta and V. Ryzhov, *Journal of Physics: Conference Series*, 2010, **200**, 012099.
- 21 B. Prasad, W. Zhang, J. Jian, H. Wang and M. G. Blamire, *Advanced Materials*, 2015, **27**, 3079-3084.
- 22 B. Prasad, M. Egilmez, F. Schoofs, T. Fix, M. E. Vickers, W. Zhang, J. Jian, H. Wang and M. G. Blamire, *Nano letters*, 2014, **14**, 2789-2793.
- 23 M. Egilmez, M. Abdelhadi, Z. Salman, K. Chow and J. Jung, *Applied Physics Letters*, 2009, **95**, 2505.
- 24 M. Kasai, H. Kuwahara, Y. Tomioka and Y. Tokura, *Journal of applied physics*, 1996, **80**, 6894-6897.
- 25 H. Oshima, K. Miyano, Y. Konishi, M. Kawasaki and Y. Tokura, *Applied physics letters*, 1999, **75**, 1473.
- 26 M. Srivastava, M. Singh, P. Siwach, A. Kaur, F. Razavi and H. Singh, *Solid State Communications*, 2012, **152**, 138-141.
- 27 M. K. Srivastava, M. Singh, A. Kaur, F. Razavi and H. Singh, *Journal of Applied Physics*, 2011, **110**, 123922.
- 28 M. K. Srivastava, P. Siwach, A. Kaur and H. K. Singh, *Magnetics, IEEE Transactions on*, 2011, **47**, 2486-2489.
- 29 E. Dagotto, *New Journal of Physics*, 2005, **7**, 67.
- 30 J. Gazquez, S. Bose, M. Sharma, M. Torija, S. J. Pennycook, C. Leighton and M. Varela, *APL Materials*, 2013, **1**, 012105.
- 31 E. M. Choi, T. Fix, A. Kursumovic, C. J. Kinane, D. Arena, S. L. Sahonta, Z. Bi, J. Xiong, L. Yan and J. S. Lee, *Advanced Functional Materials*, 2014, **24**, 7478-7487.
- 32 E.-M. Choi, A. Kursumovic, O. J. Lee, J. e. E. Kleibeuker, A. Chen, W. Zhang, H. Wang and J. L. MacManus-Driscoll, *ACS applied materials & interfaces*, 2014, **6**, 14836-14843.
- 33 M. Singh, K. Truong, P. Fournier, P. Rauwel, E. Rauwel, L. Carignan and D. Ménard, *Applied Physics Letters*, 2008, **92**, 112505-112505.
- 34 K. Ueda, Y. Muraoka, H. Tabata and T. Kawai, *Applied Physics Letters*, 2001, **78**, 512.
- 35 D. Dunstan, S. Young and R. Dixon, *Journal of applied physics*, 1991, **70**, 3038-3045.
- 36 A. Kurbakov, C. Martin and A. Maignan, *Physics of the Solid State*, 2008, **50**, 275-282.
- 37 J. L. MacManus-Driscoll, P. Zerrer, H. Wang, H. Yang, J. Yoon, A. Fouchet, R. Yu, M. G. Blamire and Q. Jia, *Nature materials*, 2008, **7**, 314-320.
- 38 D. S. Gunn, N. L. Allan and J. A. Purton, *Journal of Materials Chemistry A*, 2014, **2**, 13407-13414.
- 39 S. Sankarajan, S. Aravindan, M. Rajkumar and V. Rajendran, *Journal of Alloys and Compounds*, 2009, **485**, 17-25.
- 40 J. MacManus-Driscoll, A. Suwardi, A. Kursumovic, Z. Bi, C.-F. Tsai, H. Wang, Q. Jia and O. J. Lee, *APL Materials*, 2015, **3**, 062507.
- 41 W. Jung and H. L. Tuller, *Energy & Environmental Science*, 2012, **5**, 5370-5378.
- 42 H. Yang, H. Wang, H. Luo, D. Feldmann, P. Dowden, R. DePaula and Q. Jia, *Applied Physics Letters*, 2008, **92**, 62905-62905.
- 43 D. Worledge, G. J. Snyder, M. Beasley, T. Geballe, R. Hiskes and S. DiCarolis, *Journal of applied physics*, 1996, **80**, 5158-5161.
- 44 R. Prasad, H. Singh, M. Singh, W. Prellier, P. Siwach and A. Kaur, *Journal of Applied Physics*, 2008, **103**, 3906.
- 45 A. Hassen and P. Mandal, *Journal of applied physics*, 2007, **101**, 113917.
- 46 C. Martin, A. Maignan, M. Hervieu and B. Raveau, *Physical Review B*, 1999, **60**, 12191.
- 47 M. K. Srivastava, S. Singh, P. Siwach, A. Kaur, V. Awana, K. Maurya and H. Singh, *AIP Advances*, 2013, **3**, 052118.
- 48 B. Nanda and S. Satpathy, *Physical Review B*, 2008, **78**, 054427.
- 49 D. Kozlenko, N. Dang, Z. Jiráč, S. Kichanov, E. Lukin, B. Savenko, L. Dubrovinsky, C. Lathe and C. Martin, *The European Physical Journal B-Condensed Matter and Complex Systems*, 2010, **77**, 407-411.
- 50 A. Sadoc, B. Mercey, C. Simon, D. Grebille, W. Prellier and M.-B. Lepetit, *Physical review letters*, 2010, **104**, 046804.